



## Full length article

## Competition between thermodynamics, kinetics and growth mode in the early-stage oxidation of an equimolar CoCrFeNi alloy

Xiao-Xiang Yu<sup>a,\*</sup>, Matthew A. Taylor<sup>b</sup>, John H. Perepezko<sup>b</sup>, Laurence D. Marks<sup>a</sup><sup>a</sup> Department of Materials Science and Engineering, Northwestern University, Evanston, IL 60208, United States<sup>b</sup> Department of Materials Science and Engineering, University of Wisconsin-Madison, Madison, WI 53706, United States

## ARTICLE INFO

## Article history:

Received 30 December 2019

Revised 24 June 2020

Accepted 27 June 2020

Available online 5 July 2020

## Keywords:

Multi-principal element alloys  
High-temperature oxidation  
Transmission electron microscopy

## ABSTRACT

We demonstrate that the early-stage oxidation of a CoCrFeNi multi-principal element alloy depends upon a competition between kinetic and thermodynamic factors involving the relative diffusion rate of cations and oxygen, and how this couples to inward or outward oxide growth. The microstructures of oxide layers formed at temperatures from 500 to 800 °C for 0.5 h, as well as their chemical compositions, were investigated by transmission electron microscopy. A triple layer microstructure with an outer Fe-rich spinel oxide, an intermediate Cr-rich corundum structure, and a Ni-rich (Fe, Co, and Cr depleted) dealloyed region at the metal/oxide interface was observed. The dominant oxygen transport in corundum at 800 °C and below led to an inward growth of the corundum phase; the spinel oxide growth was dominated by cation diffusion, so it grew outward. The chromium was sequestered in the corundum layer, thereby favoring the formation of the chromium-free, Fe-rich spinel oxides with Co and Ni dopants. Since nickel cannot readily diffuse through corundum, it tends to remain in the alloy phase leading to the Ni-rich dealloyed region at the metal/oxide interface. Beyond the microstructure results, we exploit secondary electron image contrast to show the doping nature of the oxides, a p-type spinel and a n-type corundum growing on the metal surface.

© 2020 Acta Materialia Inc. Published by Elsevier Ltd. All rights reserved.

## 1. Introduction

Conventional alloy design in the past has been constrained to one or two principal components plus some minor alloying elements. The compositions are well developed close to the corner and edge of the multi-component phase diagram, with little knowledge about the compositions at the center. Multi-principal element alloys (MPEAs), also known as high-entropy alloys (HEAs), have drawn much attention over the last decade due to various interesting and unusual properties [1–9]. The most frequently used elements in MPEAs so far include Fe, Ni, Cr, Co, and Mn [10], the equiatomic CoCrFeMnNi, also called the Cantor alloy [11] has been the subject of extensive work in the field. While significant work has focused on the microstructures and mechanical properties of MPEAs, much less work has been done to develop a fundamental understanding of the oxidation and corrosion behaviors [12]. Since oxidation resistance is usually an essential requirement for alloys designed for extreme environments, the vast compositional space and numerous combinations of constituents in MPEAs offer an opportunity to reduce oxidation by new approaches, e.g. [13–17].

To date, several studies on the long-term oxidation (a few to thousands of hours) of the Cantor alloy and its variations at high temperatures have been published [18–26]. A deterioration of oxidation resistance due to nonprotective Mn oxides was observed at 500–1100 °C in laboratory air, indicating that lower amounts of Mn should be pursued for high-temperature applications [19,22,25]. Consistent with this, the oxidation resistance of CoCrFeNi (with minor Mn) was found to be comparable to a commercial austenitic stainless steel 304H at 650 °C, and slightly worse at 750 °C [21]. In terms of the oxidation kinetics, Kai et al. [18] observed complex and temperature-dependent forms for a CoCrFeNi quaternary alloy, following a single-stage parabolic rate law at 800 °C, a two-stage parabolic rate law at 850 °C, and a three-stage parabolic kinetics at 900 and 1000 °C. While only a single Cr<sub>2</sub>O<sub>3</sub> layer was reported for 15 min exposure at 1000 °C, triplex scales formed after 72 h oxidation, which consisted of an outer layer of Fe<sub>3</sub>O<sub>4</sub> and CoCr<sub>2</sub>O<sub>4</sub>, an intermediate layer of FeCr<sub>2</sub>O<sub>4</sub> and NiCr<sub>2</sub>O<sub>4</sub>, and an inner layer of Cr<sub>2</sub>O<sub>3</sub>; we will return to explain this later.

One can expect MPEAs to form complex oxides combinations and, perhaps, compositions during oxidation. The multi-stage oxidation kinetics and the temperature dependence should be related to the microstructures and compositions of oxides; however, limited information has been provided to date [23,24]. In particular,

\* Corresponding author.

E-mail addresses: [yuxx07@gmail.com](mailto:yuxx07@gmail.com), [xiaoxiang.yu@northwestern.edu](mailto:xiaoxiang.yu@northwestern.edu) (X.-X. Yu).

it is not clear whether just measurements of the weight gain/loss and the oxides present after extended time are representative of the whole process taking place. Do the same oxides form at the earliest time and/or are there changes, perhaps involving oxide–oxide reactions? Are the kinetics of the oxides different, or even their growth modes? How does varying the temperature change the kinetics?

In this paper, the microstructures of oxide layers formed on an equimolar CoCrFeNi alloy at temperatures from 500 to 800 °C for 0.5 h, as well as their chemical compositions, were investigated by transmission electron microscopy (TEM), which provides more details about how the oxides initiate and evolve. The collective results show that the early-stage oxidation depends on a competition between thermodynamics and kinetics involving the relative diffusion rate of cations and oxygen, and how this couples to inward or outward oxide growth.

## 2. Experimental details

A CoCrFeNi equimolar alloy was prepared from pure components (>99.99%) in shot form (1–2 mm) by arc melting in a Ti gettered Ar atmosphere. The sample was melted five times and flipped between each melt to ensure homogeneity. The overall weight change after ingot melting was less than 1%. The as-casted button was encapsulated in a quartz tube filled with Argon gas to avoid oxidation during heat treatment. Then the sample was annealed at 1000 °C for 24 h in a Lindberg tube furnace followed by water quenching. Several slices were cut from the inner part of the annealed button and mechanically polished using successively finer sizes of silicon carbide abrasive papers up to 1200 grit, 3 µm, and 1 µm diamond suspensions. The final stage polishing was performed by a 0.06 µm Al<sub>2</sub>O<sub>3</sub> particles slurry. Then the samples were oxidized at temperatures from 500 to 800 °C in the flowing oxygen gas (0.5 atm) for 0.5 h.

Secondary electron images were acquired by an FEI Quanta 650 scanning electron microscope using a voltage of 30 kV. The cross-sectional TEM samples were lifted out after the deposition of Pt protective layers on the oxidized surface in an FEI Helios Nanolab focused ion beam instrument, and then thinned using beam energy of 30 kV. A final cleaning step was performed at low energy (2 kV) to reduce the amorphous layer thickness. Atomic resolution scanning transmission electron microscope (STEM) imaging was performed using an aberration-corrected JEOL ARM200CF with collections angles  $\beta$  of  $11\text{ mrad} \leq \beta \leq 22\text{ mrad}$  for the annular bright field (ABF) imaging and  $90\text{ mrad} \leq \beta \leq 220\text{ mrad}$  for the high angle annular dark field (HAADF) imaging, these being acquired simultaneously. Compositional analysis was performed with a Gatan GIF spectrometer and dual silicon drift detector EDS attached to the ARM200CF.

## 3. Results

The grain size of the as-cast sample is about 200 µm with a single fcc phase, as shown in the EBSD Inverse Pole Fig. 1(a), Euler angles map Fig. 1(b), and phase map Fig. 1(c). After annealing, the as-cast dendritic microstructure is removed, and the microstructure retains the fcc phase, as confirmed by both XRD and EBSD (Fig. 1(d)–(f)). As a result, the oxidation exposures are conducted on a stable fcc phase microstructure. Grain growth is observed, and some annealing twins form in the grains, as seen in Fig. 1(e). The lattice parameter is 3.57 Å, which is consistent with other reports [27,28].

Fig. 2(a) shows the typical microstructures of oxides after oxidation at 800 °C for 0.5 h. The oxide layers consist of inner corundum and outer spinel structures, which were determined by electron diffractions. Although the thicknesses of the oxide layer vary

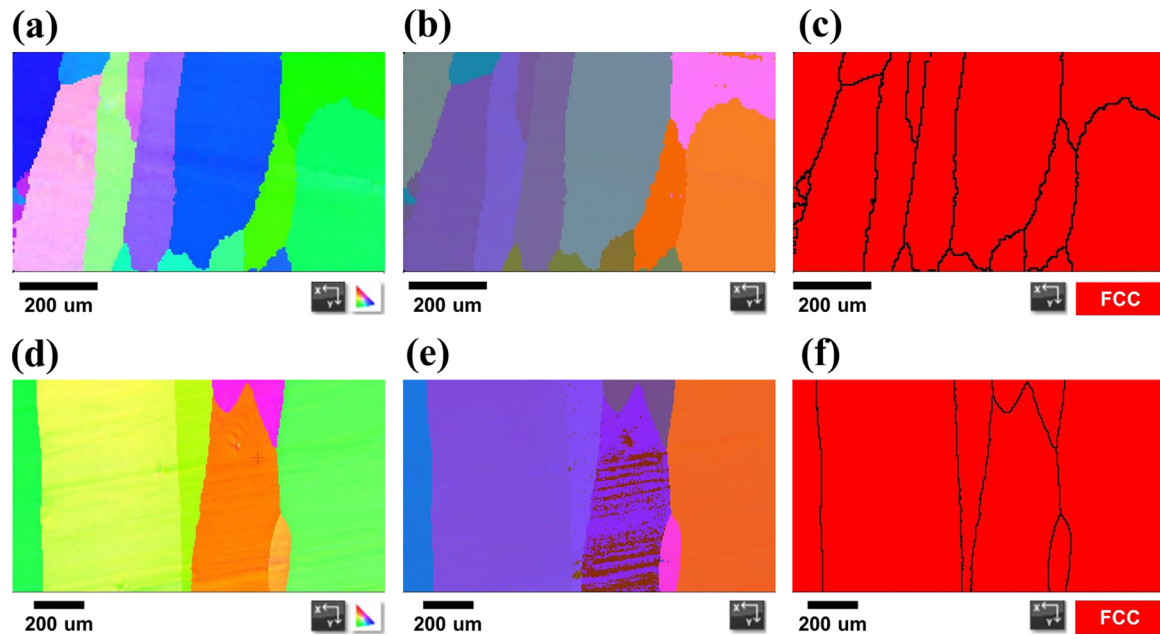
over the temperature ranges, the microstructure and constitution of the phases do not change significantly. From the compositional line scan in Fig. 2(b) and the EDS mapping in Fig. 2(c), there are three distinct regions. Nickel is abundant at the metal/oxide interface, while Cr and Fe are depleted. Chromium dominates in the corundum layer, and Fe is rich in the spinel phase. Besides Fe cations, the spinel layer also contains Co and Ni cations. Nonequilibrium solute capture [29] of nickel is found near both the metal/corundum and corundum/spinel interfaces – there is excess nickel near the corundum/metal interface, which significantly exceeds the equilibrium thermodynamic bulk solubility (~0.5 at%) of Ni in Cr<sub>2</sub>O<sub>3</sub> [30]. There is also significant Co in the corundum layer, which is not unexpected – Co and Cr form a continuous solid corundum solution Co<sub>2-x</sub>Cr<sub>x</sub>O<sub>3</sub> [31] for x less than ~4/3.

Fig. 3 shows further details of the atomic structures of the oxides for a sample oxidized at 700 °C based upon HAADF imaging. Fig. 3(a) is a lower magnification image, with the brighter (higher mass-density) region at the bottom of the alloy. Fig. 3(b) shows the corundum/Ni-rich interfacial region, where the alloy composition is reduced to an fcc Ni-based solid solution rather than an MPEA, as demonstrated by the compositional analysis in Fig. 2. The dealloyed region ranges from several to hundreds of nanometers and depends on the temperature as we show later. At all the temperatures, the corundum layers are adjacent to the metal surfaces, as shown in Fig. 3(c). In the corundum layer, at the metal/oxide interface, there are also a few isolated patches of Ni and Cr rich spinel phase, as shown in Fig. 3(d), a magnified view of the red region in Fig. 3(a).

Significant information is available from the morphology of the layered oxide; we will describe the results first, then we will turn to what these reveal. At 500 °C, the oxide shows primarily inward island growth under a flat oxide film in Fig. 4(a). The top flat oxide layer is a duplex of spinel and corundum phases. EDS mapping in Fig. 5 shows that Co and Fe are rich in the outer layer, and Cr is predominantly in the inner layer. Under the flat spinel-corundum double layer, corundum islands nucleated and grew. The size of the island was temperature-dependent, becoming larger and deeper at 600 °C with a higher nucleation density, Fig. 4(b). We note that there was a step bunch formed at the bottom right of the inward island (labeled by the white dash line and arrow in Fig. 5), indicating that the steps nucleated at the corner of the island and then propagated across the oxide/metal interface for the island growth. It is interesting that one moving step bunch was frozen during the lab air cooling under the current experimental conditions, which means that the step velocity is not extremely high. Meanwhile, O and Cr atoms segregate at the step bunch; Co and Fe are depleted, and Ni is rich on the metal side. The collective results show the growth front of the corundum island is at the oxide/metal interface.

Further information is provided in the secondary electron images in Fig. 6. In these images the corundum phase is dark (as will be explained later), the spinel is lighter. At 500 °C for 0.5 h, the spinel layer is thin; we can see the inward corundum islands from the dark contrast in the SEM images, Fig. 6(a). A few spinel islands grow out, showing in the bright contrast. As temperature increases, spinel islands grow and get coarser. From the composition, the spinel is a mixed ferrite Ni<sub>x</sub>Co<sub>1-x</sub>Fe<sub>2</sub>O<sub>4</sub>.

For each sample, the content of Ni in the spinel and the thickness of each oxide layer were measured for at least ten positions in the TEM cross-section sample by STEM-EDS line profile, such as in Fig. 2(b). The measurements were then averaged over all the positions for each sample, and the error bar shows the deviation. The thickness of the flat corundum area was measured, and the depth of inward corundum islands was not considered for the samples oxidized at 500 and 600 °C, considering the inward islands contribute minor to the overall volume of corundum layer.



**Fig. 1.** EBSD (a) IPF Z map, (b) Euler map, and (c) Phase map of the as-cast sample. (d) IPF Z map, (e) Euler map, and (f) Phase map of the sample after annealing at 1000 °C for 24 h. The grain boundaries in black are overlaid on the phase maps.

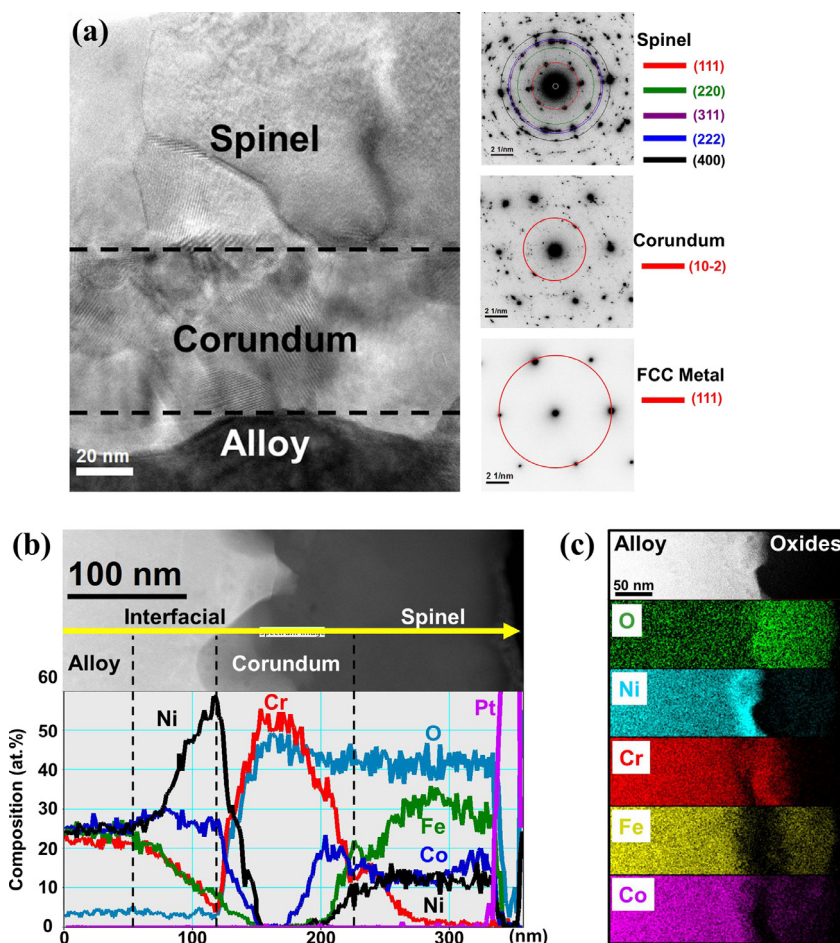


**Fig. 2.** Oxide microstructure and composition for a sample oxidized at 800 °C for 0.5 h in the flowing O<sub>2</sub> (0.5 atm). (a) HREM image shows a typical oxide microstructure consisting of an outer spinel and an inner corundum layers, as confirmed by electron diffractions. (b) EDS line profile shows three distinct regions after oxidation. (c) EDS mapping shows the distribution of each element.

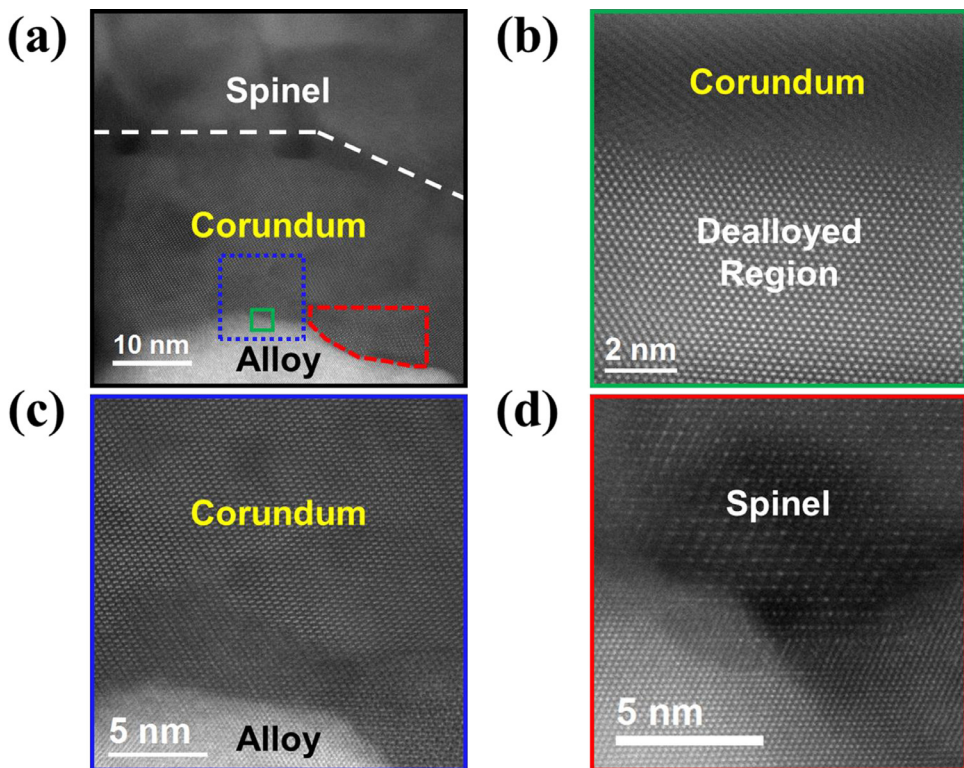


**Fig. 3.** HAADF images of oxide layers for a sample oxidized at 700 °C for 0.5 h. (a) Structures of the oxides, including an outer spinel and an inner corundum layers. Ni and Cr rich spinel phase in the corundum layer at the metal/oxide interface is marked in red. The dealloyed region at the metal/oxide interface is marked in blue. (b) A magnified view of the area marked in green in (a) showing that the dealloyed region at the metal/oxide interface has an fcc structure, (c) Corundum structure directly grows on the metal surface marked in blue in (a). (d) A small amount of spinel phase in the corundum layer, a magnified view of the area marked in red in (a). (For interpretation of the references to color in this figure legend, the reader is referred to the web version of this article.)

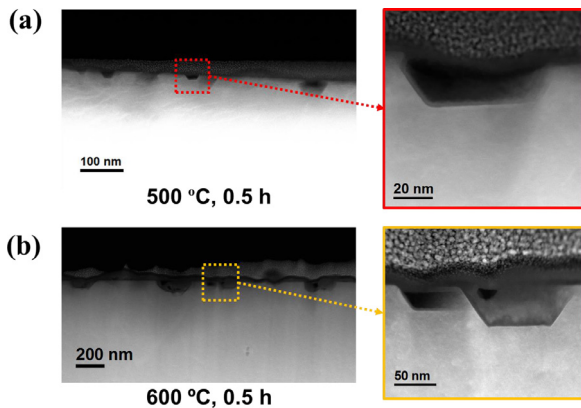


**Fig. 4.** Inward growth island is found at (a) 500 °C and (b) 600 °C for 0.5 h. The location of the oxide is shown in Fig. 5.

The content of Ni in the spinel in Fig. 6(b) increases with the temperature, which indicates that more Ni cations are transported through the corundum layer and incorporated into the  $\text{Ni}_x\text{Co}_{1-x}\text{Fe}_2\text{O}_4$  phase while retaining the spinel structure. Fig. 6(c) shows the thickness of each layer with temperature—the oxide thickness changes close to linear from 600 to 800 °C. The dealloyed region also becomes significantly thicker beyond 700 °C. Fig. 6(d) plots the natural logarithm of thickness with the inverse of temperature T. By linear fitting the data and listing the coefficient of determination  $R^2$  in Table 1; we can see the oxide kinetics follow the Arrhenius temperature dependence, while Ni-rich dealloyed region is apparently away from the linear relation with  $R^2=0.8$ , whereas the  $R^2$  of other regions are beyond 0.94. From the slope of

the linear fitting, we can also get the resulting activation energies for the linear and parabolic kinetics, as listed in Table 1. Although the current data is not enough to distinguish the parabolic and linear kinetics for each layer, we will discuss the kinetics based on the dominated diffusing species and energy barriers in Section 4.

#### 4. Analysis of the results and discussion

##### 4.1. Growth mode

It is well established that whether an oxide grows into a metal or out of it depends mainly upon what species dominate diffusion [32]; if oxygen diffusion dominates, the oxide grows inwards (with, if required by volume change, some outward expansion), whereas if cation diffusion dominates, then the oxide grows outwards. Growth can be any of flat (Frank-van der Merwe), flat+islands (Stranski-Krastanov), or islands (Volmer-Weber). Oxygen strongly chemisorbs on these electropositive metals, so only flat or flat+islands will occur – pure island growth without at least a monolayer of oxygen chemisorbed on the surface is unreasonable. Initially, one expects the oxide in both cases to be relatively flat, with stresses due to lattice misfit between the oxide and alloy so long as the misfit is not too large (when standard Volmer-Weber oxide growth would occur). Beyond some critical thickness (which could be very small), a morphological instability will develop, leading to a layer-plus-island or Stranski-Krastanov growth mode [33–35]. While the stabilizing terms for the morphological instability differ, i.e., it is the oxide/gas interfacial energy for outward growth or the oxide/alloy interfacial energy for inward growth, the mathematics are otherwise very similar [36], and this is supported by experimental data [37–39]. The shape of the islands will tend towards a Winterbottom shape [40] for outward growth; an inverse

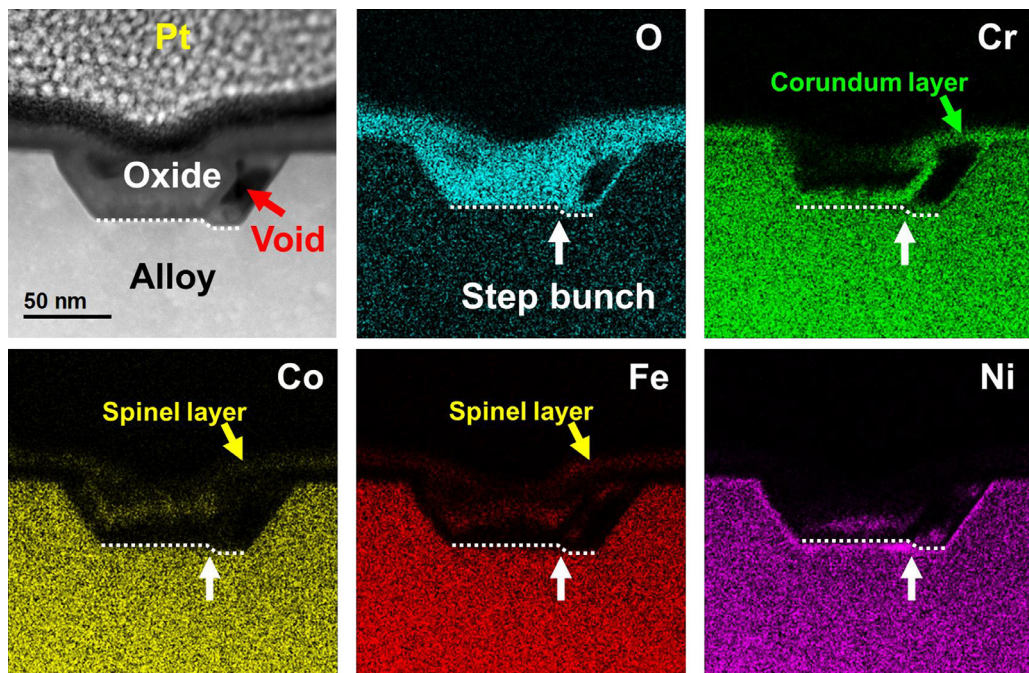


**Fig. 5.** EDS mapping of flat oxide thin film and inward growth island at 600 °C. Step bunch formed at the right corner of the island and was labeled by the white dash line and arrow. A void formed at the spinel/corundum interface is indicated by a red arrow. (For interpretation of the references to color in this figure legend, the reader is referred to the web version of this article.)

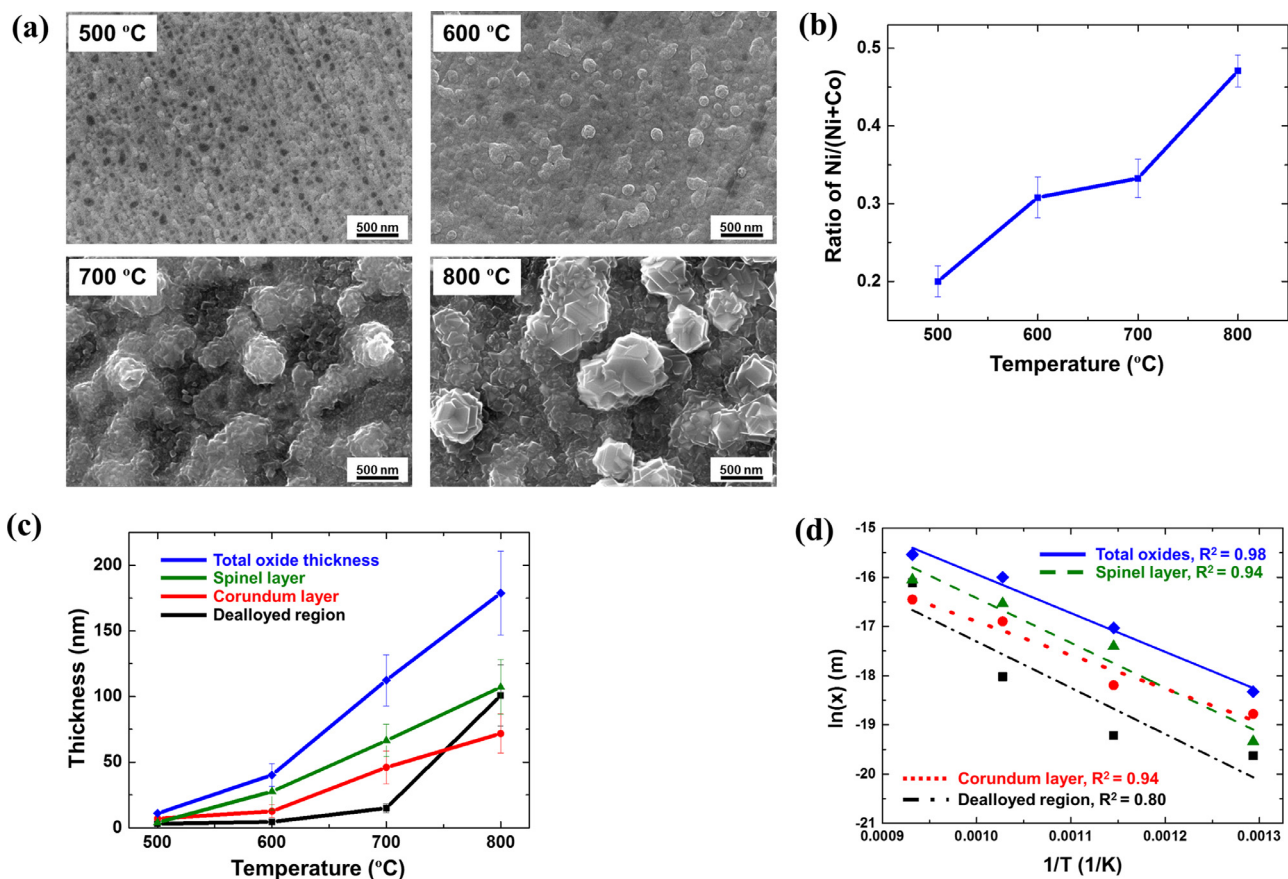


**Fig. 6.** (a) SEM images showing the oxide morphologies after oxidation at different temperatures. (b) The fraction of Ni over the total Ni and Co in the outer spinel layer with temperature. (c) The thickness of each oxide layer and the dealloyed region, as well as the total oxide thickness (spinel+corundum). (d) The natural logarithm of thickness with the inverse of temperature T. The linear fitting and the coefficient of determination  $R^2$  are also shown for each layer.

**Table 1**

Coefficient of determination  $R^2$ , activation energies for the linear and parabolic kinetics by fitting the natural logarithm of thickness with the inverse of temperature  $T$ .

	Dealloyed region	Corundum	Spinel	Total oxides
Coefficient of determination $R^2$	0.80	0.94	0.94	0.98
Activation energy for the linear kinetics (eV)	0.81	0.59	0.78	0.68
Activation energy for the parabolic kinetics (eV)	1.62	1.18	1.57	1.36

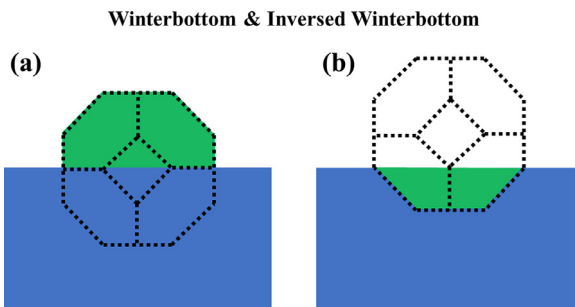


**Fig. 7.** Schematic diagram of Winterbottom (a) and Inverse Winterbottom (b). These are the kinetic shapes for islands growing in (a) away from a flat interface and in (b) inwards from a flat interface. In both cases, the islands are green, and the substrate is blue. (For interpretation of the references to color in this figure legend, the reader is referred to the web version of this article.)

Winterbottom shape for inward growth, as illustrated in Fig. 7; we will return a little later to explain this further.

It is established that oxygen diffusion dominates in the corundum structure [41–43] in the current temperature range, consistent with inward growth and an inverse Winterbottom shape. The reported migration barriers for oxygen vacancy-mediated diffusion in corundum is 1.22 eV [44], which is close to the activation energy for the parabolic kinetic value of 1.17 eV in Table 1, indicating the corundum layer follows the parabolic kinetics. What oxygen species is involved is currently not completely clear. While it could be conventional oxygen vacancies, there is also evidence that neutral oxygen interstitials (e.g. [45–50]), which are best described as peroxide ions ( $O_2^{2-}$ ) could also be involved in the transport. With structures such as corundum, there is more open space due to the partial occupancy of the octahedral sites available to cations, so neutral oxygen interstitials can be low energy defects. With regard to the spinel layer, unfortunately, there is minimal data on the details of the diffusing species. Since it is known for other, simpler spinels [51,52] that cation disorder can have a significant effect, and there may well be considerable disorder in these spinels, we cannot rely upon prior measurements. However, it is clear from the results and, in particular, at the higher temperatures in Fig. 6 that the spinel is growing outwards, indicating dominance by cation diffusion. In the literature, the Fe cation diffusion barrier in a  $\text{CoFe}_2\text{O}_4$  spinel is 0.96 eV, while that for Co is 0.83 eV [53]. These do not match the value of 1.57 eV for parabolic kinetics in the spinel layer (Table 1), but the Co value is close to the value of 0.78 eV for the linear kinetic activation energy in Table 1, which indicates the spinel layer may follow the linear kinetics.

Also, pores and voids are found at the interface of the spinel-corundum double layer in Figs. 3a, 4 and 5 (where we have labeled one of them), as well as the graphical abstract. The positions of those pores strongly indicate the condensation and coalescence of cation vacancies into voids during the spinel growth because of the cation (Fe, Co, Ni) outward diffusion. The pores and voids continue to serve as the open space for inward oxygen diffusion and corundum forms beneath. While the adhesion of corundum on metal is much better without evident voids formation, the observations

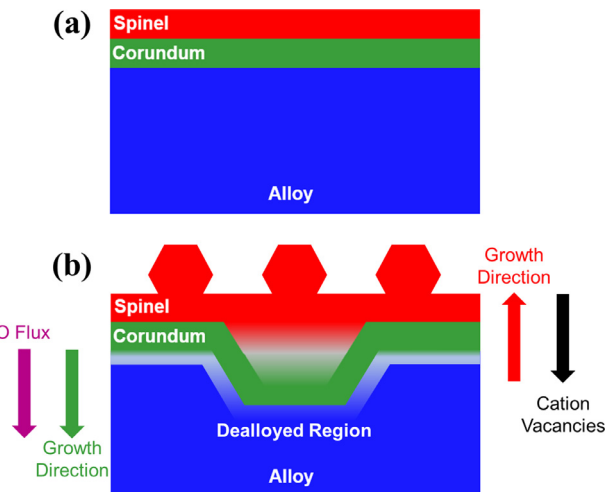


**Fig. 8.** Schematic diagram of inward corundum island formation at the metal/oxide interface. Initially somewhat flat corundum and spinel layers form as shown in (a), and then evolve towards island growth of Winterbottom shapes on top of the spinel and inverse Winterbottom shapes for the corundum.

agree well with the inward oxygen diffusion in corundum we propose beforementioned.

The process of the island formation is illustrated in Fig. 8. In the beginning, the duplex spinel and corundum layers are flat. At some point, the island forms at the corundum/metal interface, and also on top of the spinel. The shape of the islands will be determined either or both by thermodynamics (i.e., when diffusion is fast), or growth kinetics. To briefly expand (see [54] and references therein), the thermodynamic equilibrium shape of a free-standing particle can be determined from the inner envelope of normal to the surface free energy, the well-known Wulff construction [55]. What is not so widely known is that the same construction is used for growth shapes using the inner envelope of normal to the growth velocities of different facets, provided that step-flow growth dominates. Indeed, the original paper by Wulff [55] was, in fact, on kinetic shapes. The case when growth velocities are used is known as the kinetic Wulff construction.

The spinel islands (see Figs. 4–7) are the classical Winterbottom shape [40], see also [54], and references therein; the corundum shapes correspond to inverse Winterbottom shapes. Similar to thermodynamic or kinetic Wulff shapes, these Winterbottom shapes are the thermodynamic or kinetic growth shapes for islands constrained to have a flat interface to a substrate. If thermodynamics control, the relevant terms are the interfacial free energies, which can be generalized as weighted mean curvatures to include stress contributions [54,56]. For kinetic control, the shapes are determined by growth velocities, which include additional growth terms at triple points [54,57]. The constraint that the substrate remains flat can be violated if thermodynamics dominate, in which case a particle on top will penetrate the substrate [58], and an inverse Winterbottom shape should not maintain a flat outer interface. In contrast, kinetic Winterbottom shapes growing inwards or outwards would maintain flat interfaces – there is no growth ve-

**Table 2**

The Gibbs formation energy of the related oxides at 1100 K [62]. The free energies are normalized by the number of metal and oxygen atoms in each phase, and the sequence of oxides are sorted by the formation energies per oxygen. The phase was observed in this work or prior [18], as indicated in the last column.

Oxide	Structure	$\Delta G_f$ (kJ/mol)	M	O	$\Delta G_f /M$	$\Delta G_f /O$	Phase observed
Ni <sub>2</sub> O <sub>3</sub>	Hexagonal	-395.6	2	3	-197.8	-131.9	
NiO	Rocksalt	-140.7	1	1	-140.7	-140.7	
CoO	Rocksalt	-156.6	1	1	-156.6	-156.6	
NiFe <sub>2</sub> O <sub>4</sub>	Spinel	-693.6	3	4	-231.2	-173.4	This work
CoFe <sub>2</sub> O <sub>4</sub>	Spinel	-708.6	3	4	-236.2	-177.1	This work
Fe <sub>2</sub> O <sub>3</sub>	Hematite	-536.0	2	3	-268.0	-178.7	
Fe <sub>3</sub> O <sub>4</sub>	Magnetite	-762.4	3	4	-254.1	-190.6	[18]
FeO	Wüstite	-200.7	1	1	-200.7	-200.7	
NiCr <sub>2</sub> O <sub>4</sub>	Spinel	-989.2	3	4	-329.7	-247.3	[18]
CoCr <sub>2</sub> O <sub>4</sub>	Spinel	-1056.2	3	4	-352.1	-264.1	[18]
FeCr <sub>2</sub> O <sub>4</sub>	Spinel	-1088.5	3	4	-362.8	-272.1	[18]
Cr <sub>2</sub> O <sub>3</sub>	Corundum	-851.1	2	3	-425.6	-283.7	[18]/This work

lacity, so they remain essentially flat. The conclusion that these are kinetic shapes is consistent with the earlier analysis that diffusion kinetics dominate the oxide growth. We have observed similar behavior in Ni-30 wt%Cr pulse oxidation experiments [59].

#### 4.2. Temperature-dependent kinetics and nonequilibrium phases

The microstructures of oxides in our early-stage oxidation at 500–800 °C are remarkably different from the scales formed after long-term exposure at temperatures beyond 900 °C [18], in which it was reported that an outer layer of Fe<sub>3</sub>O<sub>4</sub> and CoCr<sub>2</sub>O<sub>4</sub>, an intermediate layer of FeCr<sub>2</sub>O<sub>4</sub> and NiCr<sub>2</sub>O<sub>4</sub>, and an inner layer of Cr<sub>2</sub>O<sub>3</sub> formed after oxidation at 900 °C for 72 h and 1000 °C for 48 h. The results are also different from the corundum reported in reference [18] for 15 min oxidation of CoCrFeNi at 1000 °C. Since all elements in the CoCrFeNi alloy possess approximately the same concentration, the free energies of the related oxides can be considered to assess their formation tendency and thermodynamic stability during oxidation. Table 2 lists the formation energies of the possible oxides at 1100 K. The free energies are normalized by the number of metal and oxygen atoms in each phase, and the sequence of oxides are sorted by the formation energies per oxygen.

Consider first the case of which oxides would be expected with an infinite supply of oxygen. These would be the most negative values per metal atom, which are corundum and the chromium-containing spinels. In an extended oxidation experiment, the growth rate at the end is slow, so the oxide (particularly the outermost oxide) will tend towards these compounds independent of what forms at early times. This conclusion is consistent with the prior literature for long-term exposures detailed in the Introduction.

However, in our temperature window for the corundum phase, oxygen diffusion dominates. This sequesters the chromium. It is known that a continuous solid solution forms in the system Fe<sub>2-x</sub>Cr<sub>x</sub>O<sub>3</sub> [60] and also Co<sub>2-x</sub>Cr<sub>x</sub>O<sub>3</sub> [31] for x less than ~4/3 involving either Fe<sup>3+</sup> or Co<sup>3+</sup>. Hence the corundum phase will be permeable to Fe and Co. Note that from Table 1, the free energy of formation of Cr<sub>2</sub>O<sub>3</sub> is significantly lower than that of Fe<sub>2</sub>O<sub>3</sub> and Co<sub>2</sub>O<sub>3</sub>. This suggests that the diffusion of Fe and/or Co in a corundum solid solution will be significantly faster than that of the host Cr cations, as activation energy barriers approximately scale with the strength of the metal-oxygen bonding. In contrast, Ni<sup>3+</sup> does not form as a substitutional species in corundum, it is reduced by Cr<sup>3+</sup> [61]. In addition, the free energy of formation of Ni<sub>2</sub>O<sub>3</sub> is significantly more positive. Therefore, the corundum acts as a partial nickel diffusion barrier. In the absence of both Cr and Ni the thermodynamically preferred phase will be the Fe/Co spinel. Note that

the change with temperature of the width of the Ni-rich dealloyed region in the metal is clearly non-linear (Fig. 6(c)).

Further support for this explanation is available from the results at 900–1000 °C using Pt-markers [18–20]. The markers were always located at the interface between the inner scale layer and the substrate, indicating that the scale grew mainly by outward diffusion of cations. The temperature above which Cr outward diffusion becomes important is about 900 °C [20,25], below which the inward oxygen diffusion dominates, and the Cr atoms are immobile. At the higher temperatures, all cations are available, which is consistent with the observation of the chromium-containing spinels.

The experimental oxide morphology indicates that inward oxygen diffusion dominates the growth of corundum; outward cation diffusion dominates that of the spinel. The non-Arrhenius temperature dependence of the width of the Ni-rich depletion layer in the metal is because that the metal is not acting (for the conditions of our experiments) as an infinite source of Cr, Fe or Co, the available concentration of these elements at the metal/oxide interface is decreasing with temperature which competes with the standard Arrhenius rate increase. In effect, the Ni-rich depletion layer is acting as a (soft) diffusion barrier.

#### 4.3. P-N junction and image contrast

In addition to phase composition, an important parameter in oxidation both at high temperatures and aqueous corrosion is the local electronic structure, including band bending and space charge. Since the original work of Cabera and Mott [63], it has been recognized that dissociative chemisorption of oxygen at oxide surfaces requires electron transfer and plays a major role in the kinetics; more details of how the crystallography and other phenomena can influence early-stage oxidation can be found in [64] and references therein. It is therefore important to understand the local band alignments of the alloy and oxides, as well as defects since the work function of the oxide (which changes with defect concentrations) plays a major role in dissociative oxygen chemisorption. As we will show below, some information on this is available in the SEM images, which show clear work-function contrast.

As seen in Fig. 6(a), the corundum islands are dark/black, the spinel islands are bright/white, and the metal surface is somewhere in the middle (gray). The contrast exhibited in the secondary electron mode between differently doped areas can be attributed to the difference in energy required for electron emission from these regions [65]. (There is also some overall topological contrast; both contribute to such images.) Corundum and spinel can be both p-type and n-type semiconductors, as determined by the major point defects that govern the oxide scale growth, which depend on temperature and oxygen partial pressure [41,66,67].

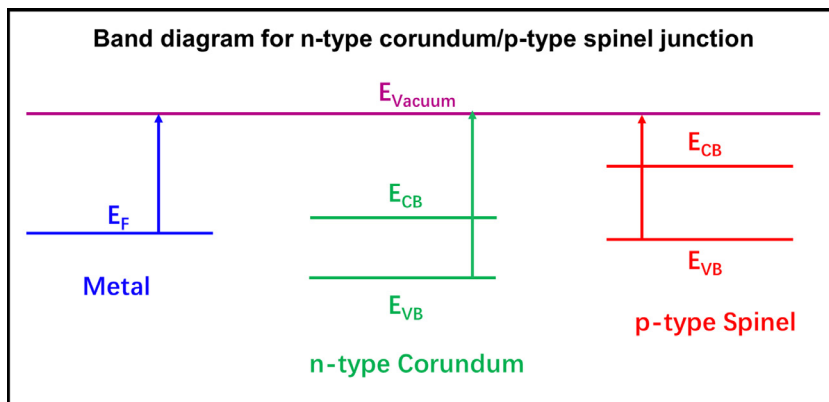


Fig. 9. Band diagram of n-type corundum/p-type spinel junction.

The major point defects in corundum are oxygen vacancies and/or interstitials leading to n-type behavior, whereas the major point defects in spinel are cation vacancies resulting in p-type behavior. The schematic band diagram of an n-type corundum/p-type spinel junction in Fig. 9 shows that extra energy is required for secondary electrons emission from n-type corundum compared to the p-type spinel. Therefore, more electrons are collected from spinel layers, contributing to the bright contrast. The SEM imaging contrast is consistent with the transport mechanisms we discussed above.

## 5. Summary

The results presented here indicate that the oxidation of a multi-component alloy is a complex process involving:

1. Inward and/or outward growth dependent upon the diffusing species, which can change with temperature.
2. Morphological instabilities in the oxide films.
3. Differing thermodynamics when specific cations are sequestered in the early forming oxides.
4. Action of certain oxides as diffusion barriers.
5. Non-equilibrium solute capture [29].

## Declaration of Competing Interest

The authors declare that they have no known competing financial interests or personal relationships that could have appeared to influence the work reported in this paper.

## Acknowledgments

The authors acknowledge support from ONR MURI “Understanding Atomic Scale Structure in Four Dimensions to Design and Control Corrosion Resistant Alloys” on Grant Number N00014-16-1-2280. We thank Mr. Chuan Liu for assistance with sample annealing.

## References

- [1] J.W. Yeh, S.K. Chen, S.J. Lin, J.Y. Gan, T.S. Chin, T.T. Shun, C.H. Tsau, S.Y. Chang, Nanostructured high-entropy alloys with multiple principal elements: novel alloy design concepts and outcomes, *Adv. Eng. Mater.* 6 (5) (2004) 299–303.
- [2] Y. Zhang, T.T. Zuo, Z. Tang, M.C. Gao, K.A. Dahmen, P.K. Liaw, Z.P. Lu, Microstructures and properties of high-entropy alloys, *Prog. Mater. Sci.* 61 (2014) 1–93.
- [3] F. Otto, A. Dlouhy, C. Somsen, H. Bei, G. Eggeler, E.P. George, The influences of temperature and microstructure on the tensile properties of a CoCrFeMnNi high-entropy alloy, *Acta Mater.* 61 (15) (2013) 5743–5755.
- [4] F. Granberg, K. Nordlund, M.W. Ullah, K. Jin, C. Lu, H. Bei, L.M. Wang, F. Djurabekova, W.J. Weber, Y. Zhang, Mechanism of radiation damage reduction in equiatomic multicomponent single phase alloys, *Phys. Rev. Lett.* 116 (13) (2016) 135504.
- [5] K.Y. Tsai, M.H. Tsai, J.W. Yeh, Sluggish diffusion in Co–Cr–Fe–Mn–Ni high-entropy alloys, *Acta Mater.* 61 (13) (2013) 4887–4897.
- [6] B. Gludovatz, A. Hohenwarter, D. Catoor, E.H. Chang, E.P. George, R.O. Ritchie, A fracture-resistant high-entropy alloy for cryogenic applications, *Science* 345 (6201) (2014) 1153–1158.
- [7] M.C. Gao, J.-W. Yeh, P.K. Liaw, Y. Zhang, *High-entropy Alloys: Fundamentals and Applications*, Springer, 2016.
- [8] B.S. Murty, J.-W. Yeh, S. Ranganathan, P. Bhattacharjee, *High-entropy Alloys*, Elsevier, 2019.
- [9] Z. Li, K.G. Pradeep, Y. Deng, D. Raabe, C.C. Tasan, Metastable high-entropy dual-phase alloys overcome the strength-ductility trade-off, *Nature* 534 (7606) (2016) 227–230.
- [10] D.B. Miracle, O.N. Senkov, A critical review of high entropy alloys and related concepts, *Acta Mater.* 122 (2017) 448–511.
- [11] B. Cantor, I.T.H. Chang, P. Knight, A.J.B. Vincent, Microstructural development in equiatomic multicomponent alloys, *Mater. Sci. Eng. A – Struct. Mater. Prop. Microstruct. Process.* 375 (2004) 213–218.
- [12] O.N. Senkov, D.B. Miracle, K.J. Chaput, J.-P. Couzine, Development and exploration of refractory high entropy alloys—a review, *J. Mater. Res.* 33 (19) (2018) 3092–3128.
- [13] P. Lu, J.E. Saal, G.B. Olson, T.S. Li, O.J. Swanson, G.S. Frankel, A.Y. Gerard, K.F. Quiambao, J.R. Scully, Computational materials design of a corrosion resistant high entropy alloy for harsh environments, *Scr. Mater.* 153 (2018) 19–22.
- [14] K.F. Quiambao, S.J. McDonnell, D.K. Schreiber, A.Y. Gerard, K.M. Freedy, P. Lu, J.E. Saal, G.S. Frankel, J.R. Scully, Passivation of a corrosion resistant high entropy alloy in non-oxidizing sulfate solutions, *Acta Mater.* 164 (2019) 362–376.
- [15] K.C. Lo, Y.J. Chang, H. Murakami, J.W. Yeh, A.C. Yeh, An oxidation resistant refractory high entropy alloy protected by CrTaO<sub>4</sub>-based oxide, *Sci. Rep.* 9 (1) (2019) 7266.
- [16] L. Backman, E.J. Opila, Thermodynamic assessment of the group IV, V and VI oxides for the design of oxidation resistant multi-principal component materials, *J. Eur. Ceram. Soc.* 39 (5) (2019) 1796–1802.
- [17] E. Osei-Agyemang, G. Balasubramanian, Surface oxidation mechanism of a refractory high-entropy alloy, *NPJ Mater. Degrad.* 3 (1) (2019) 1–8.
- [18] W. Kai, W.L. Jang, R.T. Huang, C.C. Lee, H.H. Hsieh, C.F. Du, Air oxidation of FeCoNi-base equi-molar alloys at 800–1000°C, *Oxid. Metals* 63 (3–4) (2005) 169–192.
- [19] W. Kai, C.C. Li, F.P. Cheng, K.P. Chu, R.T. Huang, L.W. Tsay, J.J. Kai, The oxidation behavior of an equimolar FeCoNiCrMn high-entropy alloy at 950°C in various oxygen-containing atmospheres, *Corros. Sci.* 108 (2016) 209–214.
- [20] W. Kai, F.P. Cheng, C.Y. Liao, C.C. Li, R.T. Huang, J.J. Kai, The oxidation behavior of the quinary FeCoNiCrSix high-entropy alloys, *Mater. Chem. Phys.* 210 (2018) 362–369.
- [21] G.R. Holcomb, J. Tylicki, C. Carney, Oxidation of CoCrFeMnNi high entropy alloys, *JOM* 67 (10) (2015) 2326–2339.
- [22] G. Laplanche, U.F. Volkert, G. Eggeler, E.P. George, Oxidation behavior of the CrMnFeCoNi high-entropy alloy, *Oxid. Metals* 85 (5–6) (2016) 629–645.
- [23] W. Kai, C.C. Li, F.P. Cheng, K.P. Chu, R.T. Huang, L.W. Tsay, J.J. Kai, Air-oxidation of FeCoNiCr-based quinary high-entropy alloys at 700–900°C, *Corros. Sci.* 121 (2017) 116–125.
- [24] N.K. Adomako, J.H. Kim, Y.T. Hyun, High-temperature oxidation behaviour of low-entropy alloy to medium- and high-entropy alloys, *J. Therm. Anal. Calorim.* 133 (1) (2018) 13–26.
- [25] Y.K. Kim, Y.A. Joo, H.S. Kim, K.A. Lee, High temperature oxidation behavior of Cr–Mn–Fe–Co–Ni high entropy alloy, *Intermetallics* 98 (2018) 45–53.
- [26] T.M. Butler, M.L. Weaver, Oxidation behavior of arc melted AlCoCrFeNi multicomponent high-entropy alloys, *J. Alloys Compd.* 674 (2016) 229–244.
- [27] K.A. Christofidou, E.J. Pickering, P. Orsatti, P.M. Mignanelli, T.J.A. Slater, H.J. Stone, N.G. Jones, On the influence of Mn on the phase stability of the CrMnxFeCoNi high entropy alloys, *Intermetallics* 92 (2018) 84–92.
- [28] C.H. Tsau, S.X. Lin, C.H. Fang, Microstructures and corrosion behaviors of Fe–CoNi and CrFeCoNi equiatomic alloys, *Mater. Chem. Phys.* 186 (2017) 534–540.

- [29] X.X. Yu, A. Gulec, Q. Sherman, K.L. Cwalina, J.R. Scully, J.H. Perepezko, P.W. Voorhees, L.D. Marks, Nonequilibrium solute capture in passivating oxide films, *Phys. Rev. Lett.* 121 (14) (2018) 145701.
- [30] J.R. Taylor, A.T. Dinsdale, A thermodynamic assessment of the Ni-O, Cr-O and Cr-Ni-O systems using the ionic liquid and compound energy models, *Z. Metall.* 81 (5) (1990) 354–366.
- [31] J.H. Chen, X.Y. Zhang, H. Arandiyani, Y. Peng, H.Z. Chang, J.H. Li, Low temperature complete combustion of methane over cobalt chromium oxides catalysts, *Catal. Today* 201 (2013) 12–18.
- [32] D.J. Young, *High Temperature Oxidation and Corrosion of Metals*, Elsevier, 2008.
- [33] A. Pimpinelli, J. Villain, *Physics of Crystal Growth*, Cambridge University Press, Cambridge, U, 1999.
- [34] J. Venables, *Introduction to Surface and Thin Film Processes*, Cambridge University Press, 2000.
- [35] K. Oura, V. Lifshits, A. Saranin, A. Zotov, M. Katayama, *Surface Science: An Introduction*, Springer Science & Business Media, 2013.
- [36] J. Tersoff, F.K. LeGoues, Competing relaxation mechanisms in strained layers, *Phys. Rev. Lett.* 72 (22) (1994) 3570–3573.
- [37] M. Bouville, J.M. Millunchick, M.L. Falk, Pit nucleation in the presence of three-dimensional islands during heteroepitaxial growth, *Phys. Rev. B* 70 (23) (2004) 235312.
- [38] C. Jang, S. Paik, Y. Kim, N.-E. Lee, Substrate pit formation and surface wetting during thermal annealing of strained-Si/relaxed-Si 0.78 Ge 0.22 heterostructure, *Appl. Phys. Lett.* 90 (9) (2007) 091915.
- [39] L. Sears, A. Riposan, J.M. Millunchick, Inverse Stranski-Krastanov growth in In-GaAs/InP, *J. Vac. Sci. Technol. A* 28 (5) (2010) 1175–1180.
- [40] W.L. Winterbottom, Equilibrium shape of a small particle in contact with a foreign substrate, *Acta Metall.* 15 (2) (1967) 303–310.
- [41] X. Ledoux, S. Mathieu, M. Vilasi, Y. Wouters, P. Del-Gallo, M. Wagner, Oxide growth characterization during short-time oxidation of a commercially available chromia-forming alloy (HR-120) in air at 1050°C, *Oxid. Metals* 80 (1–2) (2013) 25–35.
- [42] A.C.S. Sabioni, E.A. Malheiros, V. Ji, F. Jomard, W.A.D. Macedo, P.L. Gastelois, Ion diffusion study in the oxide layers due to oxidation of AISI 439 ferritic stainless steel, *Oxid. Metals* 81 (3–4) (2014) 407–419.
- [43] S. Voynnis, A. Seyeux, S. Zanna, B. Martin-Cabanas, T. Couvant, P. Marcus, Oxide layer growth on nickel-base alloy surfaces in high temperature water and in O<sub>2</sub> studied by ToF-SIMS with isotopic tracers, *Corros. Sci.* 145 (2018) 212–219.
- [44] B.K. Medasani, M.L. Sushko, K.M. Rosso, D.K. Schreiber, S.M. Bruemmer, Temperature dependence of self-diffusion in Cr<sub>2</sub>O<sub>3</sub> from first principles, *J. Phys. Chem. C* 123 (36) (2019) 22139–22150.
- [45] D.J. Buttrey, P. Ganguly, J.M. Honig, C.N.R. Rao, R.R. Schartman, G.N. Subbanna, Oxygen excess in layered lanthanide nickelates, *J. Solid State Chem.* 74 (2) (1988) 233–238.
- [46] F. Cordero, C.R. Grandini, R. Cantelli, Structure, mobility and clustering of interstitial O in La<sub>2</sub>CuO<sub>4+delta</sub> in the limit of small delta, *Physica C* 305 (3–4) (1998) 251–261.
- [47] A.S. Foster, A.L. Shluger, R.M. Nieminen, Mechanism of interstitial oxygen diffusion in hafnia, *Phys. Rev. Lett.* 89 (22) (2002) 225901.
- [48] H.Y. Xiao, Y. Zhang, W.J. Weber, Stability and migration of charged oxygen interstitials in ThO<sub>2</sub> and CeO<sub>2</sub>, *Acta Mater.* 61 (20) (2013) 7639–7645.
- [49] B. Medasani, M.L. Sushko, K.M. Rosso, D.K. Schreiber, S.M. Bruemmer, First-principles investigation of native interstitial diffusion in Cr<sub>2</sub>O<sub>3</sub>, *J. Phys. Chem. C* 122 (24) (2018) 12984–12993.
- [50] S.Z. Xu, R. Jacobs, D. Morgan, Factors Controlling Oxygen interstitial diffusion in the ruddlesden-popper oxide La<sub>2-x</sub>SrxNiO<sub>4+delta</sub>, *Chem. Mater.* 30 (20) (2018) 7166–7177.
- [51] B.P. Uberuaga, D. Bacorisen, R. Smith, J.A. Ball, R.W. Grimes, A.F. Voter, K.E. Sickafus, Defect kinetics in spinels: long-time simulations of MgAl<sub>2</sub>O<sub>4</sub>, MgGa<sub>2</sub>O<sub>4</sub>, and MgIn<sub>2</sub>O<sub>4</sub>, *Phys. Rev. B* 75 (10) (2007) 104116.
- [52] B.P. Uberuaga, G. Pilania, Effect of cation ordering on oxygen vacancy diffusion pathways in double perovskites, *Chem. Mater.* 27 (14) (2015) 5020–5026.
- [53] C.L. Muñich, V.J. Aston, R.M. Trottier, A.W. Weimer, C.B. Musgrave, First-principles analysis of cation diffusion in mixed metal ferrite spinels, *Chem. Mater.* 28 (1) (2016) 214–226.
- [54] L.D. Marks, L. Peng, Nanoparticle shape, thermodynamics and kinetics, *J. Phys. Condens Matter* 28 (5) (2016) 053001.
- [55] G. Wulff, On the question of speed of growth and dissolution of crystal surfaces, *Z. Kryst. Mineral.* 34 (5/6) (1901) 449–530.
- [56] J.E. Taylor, Mean-curvature and weighted mean-curvature. 2, *Acta Metall. Mater.* 40 (7) (1992) 1475–1485.
- [57] E. Ringe, R.P. Van Duyne, L.D. Marks, Kinetic and thermodynamic modified Wulff constructions for twinned nanoparticles, *J. Phys. Chem. C* 117 (31) (2013) 15859–15870.
- [58] P.M. Ajayan, L.D. Marks, Evidence for Sinking of small particles into substrates and implications for heterogeneous catalysis, *Nature* 338 (6211) (1989) 139–141.
- [59] X.-X. Yu, J.H. Perepezko, L.D. Marks, Crystallographic anisotropy of nonequilibrium solute capture, Submitted for publication (2020).
- [60] A. Muan, S. Somiya, Phase Relations in the System Iron Oxide-Cr<sub>2</sub>O<sub>3</sub> in Air, *J. Am. Ceram. Soc.* 43 (4) (1960) 204–209.
- [61] Q.C. Sherman, P.W. Voorhees, L.D. Marks, Thermodynamics of solute capture during the oxidation of multicomponent metals, *Acta Mater.* 181 (2019) 584–594.
- [62] I. Barin, *Thermochemical Data of Pure Substances*, VCH, 1989.
- [63] N. Cabrera, N.F. Mott, Theory of the oxidation of metals, *Rep. Prog. Phys.* 12 (1948) 163–184.
- [64] X.-X. Yu, L.D. Marks, Combining the physics of metal/oxide heterostructure, interface dipole, band bending, crystallography, and surface state to understand heterogeneity contrast in oxidation and corrosion, *Corrosion* 75 (2) (2018) 152–166.
- [65] C.P. Sealy, M.R. Castell, P.R. Wilshaw, Mechanism for secondary electron dopant contrast in the SEM, *J. Electron. Microsc.* 49 (2) (2000) 311–321.
- [66] L. Latu-Romain, Y. Parsa, S. Mathieu, M. Vilasi, M. Ollivier, A. Galerie, Y. Wouters, Duplex n- and p-type chromia grown on pure chromium: a photoelectrochemical and microscopic study, *Oxid. Metals* 86 (5–6) (2016) 497–509.
- [67] L. Latu-Romain, S. Mathieu, M. Vilasi, G. Renou, S. Coindeau, A. Galerie, Y. Wouters, The role of oxygen partial pressure on the nature of the oxide scale on a NiCr model alloy, *Oxid. Metals* 88 (3–4) (2017) 481–493.